

# The Sensitivity of Hybrid Differential Stereoscopy for Spectral Imaging

C.E. DeForest and C.C. Kankelborg

## Abstract

Stereoscopic spectral imaging is an observing technique that affords rapid acquisition of limited spectral information over an entire image plane simultaneously. Light from a telescope is dispersed into multiple spectral orders, which are imaged separately, and two or more of the dispersed images are combined using an analogy between the  $(x, y, \lambda)$  spectral data space and conventional  $(x, y, z)$  three-space. Because no photons are deliberately destroyed during image acquisition, the technique is much more photon-efficient in some observing regimes than existing techniques such as scanned-filtergraph or scanned-slit spectral imaging. Hybrid differential stereoscopy, which uses a combination of conventional cross-correlation stereoscopy and linear approximation theory to extract the central wavelength of a spectral line, has been used to produce solar Stokes-V (line-of-sight) magnetograms in the 617.34 nm Fe I line, and more sophisticated inversion techniques are currently being used to derive Doppler and line separation data from EUV images of the solar corona collected in the neighboring lines of He-II and Si-XI at 30.4 nm. In this paper we develop an analytic *a priori* treatment of noise in the line shift signal derived from hybrid differential stereoscopy. We use the analysis to estimate the noise level and measurement precision in a high resolution solar magnetograph based on stereoscopic spectral imaging, compare those estimates to a test observation made in 2003, and discuss implications for future instruments.

*Subject headings:* instrumentation: spectrographs, methods: analytical, techniques: spectroscopic

## 1. Introduction

Spectral imaging in general, and solar spectral imaging in particular, suffer from a fundamental problem in detector physics. Spectral images have three independent variables  $(x, y, \lambda)$ , while current image detectors only support two independent variables  $(x, y)$  and integrate over wavelength  $\lambda$ . Conventional techniques to overcome this problem generally use time-multiplexing: in filtergraph imaging spectroscopy, a narrow band filter is tuned slowly across the spectral range

of interest and an image collected at each discrete  $\lambda$ ; in conventional scanned-slit imaging spectroscopy, the light is passed through a spatial filter (the slit), selecting a single  $x$ , and the remaining light is dispersed to project  $\lambda$  onto the detector's  $x$  axis. Even more sophisticated techniques such as Fourier imaging spectroscopy use time multiplexing to collect multiple two-dimensional basis images of the three-dimensional data space. Multiplexing in time is photon-inefficient as photons that are not part of the current sample are discarded. That is a problem because solar measurements are photon starved: instruments must race to collect sufficient photons for a spectral measurement, before the features on the Sun change.

Stereoscopic spectral imaging overcomes the problem of spectral imaging by analogy between the spectral imaging problem and the stereoscopic problem of determining feature distance in ordinary 3-space. Dispersed spectral images are integrals along diagonal lines in  $(x, y, \lambda)$  space; they are analogous to images of a 3-space subject, with the images collected at a “look angle” that depends on the dispersion of the instrument. Collecting multiple dispersed images in different spectral orders yields data that can be inverted stereoscopically to measure some spectral characteristics of the line everywhere in the image plane simultaneously.

Kankelborg et al. (2001) and Fox et al. (2003) have described using this stereoscopic approach to simultaneous imaging and spectroscopy in EUV emission lines. Their *MOSES* rocket payload, launched 2006 February 8, obtained Doppler measurements of explosive events and jets in the He II line at 30.4 nm (Kankelborg and Fox 2007). Another related technique, computed-tomography imaging spectroscopy (CTIS) uses multiple spectral orders for hyperspectral imaging and spectropolarimetry at low spectral resolution in the visible and infrared (e.g. Wilson et al. 1997; Miles 1999; Miles et al. 1999; Dereniak 2005).

DeForest et al. (2004) have developed a first-order theory of stereoscopic inversion that is applicable to a much simpler spectral context: measuring Doppler shift and the longitudinal Zeeman splitting in a narrow visible absorption line in the solar photosphere. That work is conceptually similar to the *MOSES* stereoscopic imaging, but there are two key differences: there is only a single spectral line in the instrument passband, and it is an absorption line; and the line width is narrower than a pixel in dispersion. DeForest et al. demonstrated the technique with proof-of-concept observations of the quiet Sun, a decayed active region, and a clean sunspot. However, in that work they did not analyze the noise characteristics of the observing and inversion technique, only report the *a posteriori* noise measured in a quiet Sun region.

In this article, we derive expressions for the *a priori* noise level (hence sensitivity) and systematic error of a stereoscopic instrument in the narrow-line regime described by DeForest et al. (2004) using hybrid differential stereoscopy to determine line shift. We use *a priori* statistical calculation to derive the effect of the dominant source of uncorrelated noise - photon counting statistics - and also address quasi-random systematic errors in the inversion using some basic as-

sumptions about the scene being viewed.

The analytic expressions are general and may be applied to stereoscopic spectrographs viewing either absorption or emission lines, but we consider them in the specific context of an absorption-line Zeeman magnetograph viewing the relative line shift between the right- and left-circular polarizations. In §2 we analyze each of several noise sources individually; in §3 the results of the individual analyses are applied to generate a noise budget for an example baseline instrument observing the quiet photosphere with  $\sim 0.1$  arc sec resolution and 0.03 arc sec pixels, in the 617.34 nm Fe I absorption line. Finally, in §4 we draw conclusions about the types of observation for which hybrid differential stereoscopic spectral imaging offers the best prospects for advances over the state of the art. Throughout the discussion we have used  $\Delta$  to indicate a single difference from the correct or expected value of the following quantity, and angle-brackets to denote RMS averages over an image.

## 2. Hybrid differential stereoscopy

Here we develop a theory of noise in a hybrid differential analysis of absorption line data. Following DeForest et al. (2004), consider an image in the  $(x, y)$  plane produced by observing, through a slitless dispersing spectrograph, a narrow absorption line of rest wavelength  $\Lambda_0$ , offset  $\Lambda'(x, y)$  from that wavelength, constant width  $\Delta\lambda$ , and integrated total intensity absorption  $L(x, y)$  over that width; limiting the wavelength range on the detector is a filter with transmission profile  $F(\lambda')$  and total admitted continuum intensity  $C(x, y)$  in the absence of the spectral line. Without loss of generality, take the dispersion direction of the spectrograph to be along the  $x$  axis and consider the images collected in the  $\pm 1$  spectral order. Then the  $y$  variation of the image drops out of the analysis and inversion may be performed independently along each line parallel to the  $x$  axis. Variations in the central wavelength of the spectral line result in spatial distortions of the images; these distortions are antisymmetric across the two spectral orders, and can be used to recover low spatial frequencies of the function  $\Lambda'(x)$  by *correlation stereoscopy*. Small patches of the images are cross-correlated to determine the offset functions  $X_{L,\pm 1}(x)$ , and the wavelength offset can then be determined by

$$\Lambda'_L = \frac{X_{L,+1} - X_{L,-1}}{2\alpha}, \quad (1)$$

where  $\alpha$  is the dispersion of the +1 order. The  $L$  subscripts refer to low spatial frequencies; the maximum spatial frequency that may be resolved by this method is determined by the patch size used for the cross-correlation. The inversion used for Eq. 1 is analogous to the inversion carried out by the human visual system, determining the  $z$  coordinate of observed objects by cross-correlating the visual fields from the left and right eye. Recovering higher spatial frequencies requires a more sophisticated inversion. DeForest (2003) and DeForest et al. (2004) developed the process of

*differential stereoscopy* to determine high spatial frequencies in  $\Lambda'$  based on first-order intensity variation in the dispersed images. The difference between the +1 and -1 order dispersed images yields several terms in first approximation order, one of which is proportional to  $d\Lambda'/dx$ . By integrating the difference signal along the  $x$  direction it is possible to recover an approximation to the high spatial frequencies  $\Lambda'_H$  throughout the image plane – because the primary detection term is to the spatial derivative, low spatial frequencies are not well measured with that technique. Furthermore, differential stereoscopy is sensitive to “leakage” of intensity and other signals into the  $d\Lambda'/dx$  measurement. These terms are proportional to  $\Lambda'$  itself and must therefore be compensated in some way in strong field regions.

By resampling the dispersed images to eliminate the spatial shifts related to  $\Lambda'_L$  before applying differential stereoscopy, it is possible to eliminate image-related noise in the differential signal, to first approximation order. The differential process is used to recover high spatial frequencies, and the low spatial frequencies are inserted via a mathematical filter. The resulting *symmetric hybrid inversion equation* for first-order stereoscopic inversion (from DeForest et al. 2004) is:

$$\Lambda'_{c1} = \int \left\{ \frac{I_{-1}(X_{L,-1}) - I_{+1}(X_{L,+1})}{\alpha(I_{+1} + I_{-1})} \frac{C}{L} - \epsilon(\Lambda'_{c1} - \Lambda'_L) \right\} dx \quad (2)$$

where  $\Lambda'_L$  is again the low-spatial-frequency component of the central-wavelength shift image, as determined by explicit cross-correlation of patches of the +1 image with corresponding regions of the -1 image,  $X_{L,-1}$ , and  $X_{L,+1}$  are again distorted spatial coordinates that use the correlation signal to remove measured offsets in the images,  $I_{\pm 1}$  is the intensity profile of each image as a function of focal-plane coordinate  $x$  or the distorted focal-plane coordinate  $X_{L,\pm 1}$ ,  $\alpha$  is the dispersion of the instrument, and  $\epsilon$  is a small convergence factor that splices the frequency spectra of the two derivation methods.

Note that Eq. 2 is implicit rather than closed-form:  $\Lambda'_{c1}$  is present both on the left hand side of the equality, and also inside the integral on the right hand side. The presence of the corrective filter term  $\epsilon(\Lambda'_{c1} - \Lambda'_L)$  is what makes Eq. 2 a *hybrid* inversion: it preserves the high spatial frequencies present in the main portion of the integrand, while forcing the low spatial frequencies in the integral to match the  $\Lambda'_L$  signal obtained by direct cross-correlation of image patches. If  $\Lambda'_L$  happens to be constant and zero, then the impulse response function of the resulting spatial filter is a decaying exponential. In practice, the integral should be performed numerically in both the positive- $x$  and negative- $x$  direction, and the two results summed. The forward integral is causal along the  $x$  axis and the reverse integral is anti-causal, so that the resulting impulse response function is symmetric in  $x$ .

The discrete form of Equation 2, then, is best calculated using the sum of two discrete filter transforms. Let  $J$  be the normalized difference image in compensated coordinates, interpolated to (integer) non-distorted pixel locations, and let  $i$  run over the pixel coordinates in the  $x$  direction.

Then  $J$  may be written:

$$J(i) \equiv \frac{I_{-1X}(i) - I_{+1X}(i)}{(I_{-1X}(i) + I_{+1X}(i))} \quad (3)$$

where the  $X$  subscript is to indicate that the  $I_{\pm 1}$  images have been interpolated so that the  $i^{\text{th}}$  pixel is found from the focal-plane location  $x_i \pm \alpha \Lambda_L(x_i)$ . In the first-order theory developed by DeForest et al. 2004,  $J$  is important because, when  $d\Lambda'/dx \ll \alpha^{-1}$ ,

$$J \sim \alpha \frac{L}{C} \frac{d\Lambda'}{dx} \quad (4)$$

which allows recovery of  $\Lambda'$  by integrating and scaling appropriately.

The integral becomes a sum of two discrete spatial filters in the *discrete symmetric hybrid inversion equation*:

$$\Lambda'_{c1}(i) = \frac{1}{2\alpha} \left( \sum_{n=0}^i \left( \left\langle \frac{C}{L} \right\rangle_{RMS} J(n) + \epsilon \Lambda'_L(n) \right) (1 - \epsilon)^{i-n} - \sum_{n=i}^{w-1} \left( \left\langle \frac{C}{L} \right\rangle_{RMS} J(n) - \epsilon \Lambda'_L(n) \right) (1 - \epsilon)^{n-i} \right) \quad (5)$$

where pixel centers are considered to exist at all integers between 0 and  $w$ , and  $\langle C/L \rangle_{RMS}$  is the average ratio of admitted continuum intensity to line absorption intensity. The  $\epsilon \Lambda'_L$  terms merely produce a smoothed version of  $\Lambda'_L$ : if  $\Lambda'_L$  were constant, and the image were infinite in extent, then each of the two summations would return exactly  $\Lambda'_L$  by the law of geometric sums. The low pass filter from this smoothing effect exactly matches the high-pass filter applied to the integral by the exponential decay term, so that the two versions of  $\Lambda'$  are combined together seamlessly. Equation 5, together with the process of cross-correlation to determine the relationship between  $X_{L,\pm 1}$  and  $x$ , is a complete discrete image inversion.

Figure 1 shows the step response of the filter described by Eq. 5, to illustrate how the different parts of the inversion work together. The step is located at position 100. The high-pass response to the differential stereoscopy signal (dark blue) is due to the interaction between the differentiation inherent in the detection method, and the “imperfect” (high-pass) integration imposed by the  $\epsilon \Lambda'_{c1}$  decay term in the integrand of Eq. 2. The exponential decay is matched by the low-pass response to the correlation stereoscopy signal (light cyan). The sum of the two signals is the value of the the RHS of Eq. 5, and reproduces the original signal. The slight overshoot of the reconstructed (magenta) curve is a discretization effect due to the phase of the Heaviside function relative to the pixel grid: a Heaviside function with the opposite phase relative to the pixel grid would yield an equal-magnitude undershoot. As with any discrete sampling filter, Eq. 5 operates best on spatial frequencies less than  $2/3$  of the pixel Nyquist frequency, because the reconstructed amplitude of those frequency components is independent of their phase relative to the pixel grid. The Heaviside function contains frequencies both below and above that limit, and the high frequencies’ reconstructed amplitude depends on phase.

In practice, errors in both the measurement of intensity and the inversion affect the analysis, so that the measured  $\Lambda'_{c1}$  is not exactly the same as  $\Lambda'$  even if the image frequency spectrum is appropriately limited. In this error analysis we consider six principal sources of error: photon counting noise,  $\langle \Delta I \rangle_{RMS}$ , that represents an additive, uncorrelated noise source at each pixel in each of the differential and correlation stereoscopy steps; misalignment noise  $\langle \Delta X_L \rangle_{RMS}$  in the cross-correlation step; the effect of intensity gradients (both  $dC/dx$  and  $dL/dx$ ) on the line shift signal; a nonzero slope  $dF/d\lambda'$  of the instrument filter transmission function  $F(\lambda')$  (the slope is assumed to be zero in Eq. 2); and an excessively high  $d\Lambda'/dx$  signal in the solar image. The first two noise sources arise (directly or indirectly) from imprecision in the measurement of  $I$  in each pixel, and the last four sources arise from the non-ideal nature of the instrument and/or the solar field being imaged. In the following subsections we treat each error source independently.

### 2.1. Photon noise in differential stereoscopy

Photon counting noise is due to uncertainty in the measured intensity  $I_{\pm 1}$  in each focal plane, through the statistics of photon counting. Each measurement does not determine intensity directly, but rather fluence of energy (or, equivalently, photon count) on each pixel during an exposure time. Intensity can be derived by knowing the size of the pixel and the length of the exposure. Each pixel measures a fluence  $\Phi$  with an uncertainty  $\Delta\Phi_{ph.}$  given by:

$$\Delta\Phi_{ph.} = \frac{hc}{\Lambda} \Delta n_{ph.} = \sqrt{\frac{hc}{\Lambda}} \Phi \quad (6)$$

so that the RMS value  $\langle \Delta I/I \rangle_{RMS} = \langle \Delta\Phi/\Phi \rangle_{RMS} = \sqrt{hc/\Lambda\Phi}$ . This effect contributes to  $\Lambda'_{c1}$  primarily via a photon noise term that must be propagated through Equation 5: the much higher photon counts in many-pixel image “patches” greatly reduce photon counting noise in the cross-correlation portion of the inversion (§2.2). The RMS photon noise contribution  $\langle \Delta_{ph}\Lambda'_{c1} \rangle_{RMS}$  is just the incoherent sum of the photon noise terms in each term on the RHS of Eq. 5. Each of those terms, in turn, is (to first order in  $\Delta_{ph}I/I$  and neglecting  $dI/dx$  for the calculation of noise in each pixel):

$$\langle \Delta_{ph}J_i \rangle_{RMS} = \sqrt{\frac{2I^2 (hc\Phi/\Lambda)}{4I^2}} = \sqrt{\frac{hc}{2\Lambda\Phi}} = \sqrt{1/2n_{ph}} \quad (7)$$

where  $n_{ph}$  is the per-exposure photon count in the corresponding pixel in each of the two orders. Eq. 7 simply reproduces the familiar behavior of incoherent counting statistics for intrinsic (normalized) quantities.

The treatment may, at first glance, appear overly simple as the individual pixels in the images are interpolated and hence do not represent individual samples of the  $\Delta_{ph}\Phi$  random variable but

rather scaled incoherent sums of adjacent samples. This is acceptable to ignore because, in the absence of strong gradients in  $dX_{L,\pm 1}/dx$  (i.e. gradients comparable to unity per pixel), the samples' noise profile is preserved by the inversion. Adjacent pixels are co-added in the discrete inversion. Under linear interpolation, adjacent interpolated fractions of the signal from each detector pixel are approximately conserved by the interpolation and added coherently in the cross-pixel sum in Eq. 5. Because addition is commutative, the noise effect of the interpolated pixels on the final sum is the same as if no interpolation had taken place, up to a negligible factor of  $(1 - \epsilon)$ . Put another way, although considering interpolation would further reduce the noise in  $J_i$  for individual pixels, co-adding  $J_i$  for adjacent pixels in the inversion eq. 5 would then include coherent cross-pixel noise terms that would exactly cancel the reduction – so we may safely choose, instead, to ignore the effects of the  $X_{L,\pm 1}$  interpolation and use incoherent sums throughout.

Carrying Eq. 7 forward through Eq. 5 yields:

$$\langle \Delta_{ph} \Lambda'_{c1} \rangle_{RMS} = \frac{1}{2\alpha} \left\langle \frac{C}{L} \right\rangle_{RMS} \sqrt{\left( \frac{1}{2n_{ph}} \right) \left( \sum_{n=0}^i (1 - \epsilon)^{2(i-n)} + \sum_{n=i}^{w-1} (1 - \epsilon)^{2(n-i)} \right)} \quad (8)$$

Neglecting any field edge effects (in other words, taking  $0 \ll i \ll w$ ) permits taking the infinite sums directly, yielding (to first order in epsilon):

$$\langle \Delta_{ph} \Lambda'_{c1} \rangle_{RMS} = \frac{1}{2\alpha} \left\langle \frac{C}{L} \right\rangle_{RMS} \sqrt{\frac{1}{2n_{ph}\epsilon}} \quad (9)$$

Thus the statistics of the differential stereoscopy step are worsened by the width of the correction term. This is reflective of the fact that random walks diverge, and is the reason for using a hybrid inversion rather than a direct integral inversion: using direct integration in Equation 5, rather than high-pass integration with correction, is equivalent to setting  $\epsilon$  to zero, which would yield an arbitrarily large amount of photon-counting noise in the individual measurements. In actual use, it is necessary to balance  $\epsilon$  and the cross correlation patch size: larger patch sizes improve correlation behavior but require smaller  $\epsilon$  and thus worsen the photon noise due to integration of the differential signal.

It is important to note that the photon noise from the discrete inversion is not independently sampled at each pixel: it is the sum of many noise terms along the  $x$  direction, so that the *difference* measurement between adjacent pixels has a much smaller noise level, yielding higher precision for small features. In particular, shifting by 1 pixel re-samples only one  $\epsilon^{th}$  of the population of random samples in the calculated  $\Lambda'_{c1}$ , reducing the photon noise by a factor of  $\sqrt{\epsilon}$  so that small features are only subject to:

$$\langle \Delta_{ph} (\Lambda'_{c1,i} - \Lambda'_{c1,j-1}) \rangle_{RMS} = \frac{1}{2\alpha} \left\langle \frac{C}{L} \right\rangle_{RMS} \sqrt{\frac{1}{2n_{ph}}}, \quad (10)$$

which is to be expected considering that the difference signal is the original signal being measured by the differential stereoscopy - the difference in measured wavelength between two adjacent pixels is simply a linearly scaled form of  $J_i$ . Differential stereoscopy is *more sensitive* to small features than to large ones, at least from the standpoint of photon statistics.

Taking “typical” values of  $\epsilon = 0.09$  (FWHM of 15 pixels),  $C/L = 10$ , and  $n_{ph} = 5 \times 10^4$  yields an absolute partial sensitivity  $\alpha \langle \Delta_{ph} \Lambda'_{c1} \rangle_{RMS} = 0.052$  pixel, and a gradient sensitivity  $\alpha \langle \Delta_{ph} (\Lambda'_{c1,j} - \Lambda'_{c1,j-1}) \rangle_{RMS} = 0.016$  (the gradient sensitivity is unitless: pixels per pixel), due to photon counting alone.

## 2.2. Photon noise in correlation stereoscopy

The second source of error in Equation 5 is misalignment in the cross correlation step that is used to derive  $X_{L,\pm 1}$  from the original images. In the 2004 derivation of Eq. 2, it was necessary to assume that the displacement of the images was small, leading to  $dI/dx$  terms that enter in first order because the +1 and -1 order intensities are measured at slightly different spatial locations. Here, we consider the effect of small misalignments due to errors in the correlation co-alignment process. In the test measurements made by DeForest et al., the cross-correlation step used a full two-dimensional patch of image around each sampled point, rather than (as in the differential stereoscopic portion of the inversion) merely the particular horizontal line surrounding each point. This is reasonable in part because the image is, in fact, a two-dimensional field rather than a collection of independent rasters; and in part because the technique was found empirically to reduce correlation “misses” and improve the image signal. Here, we consider the potential sources of error injected by cross-correlation alignment of patches of image around each point.

Because correlation co-alignment is a nonlinear process and depends on the field in the image, it is necessary to make some assumptions about the field being viewed. We here confine our analysis to magnetic measurements of the quiet Sun, which consists principally of nearly uniformly bright granules separated by dark, well defined lanes. Some other types of field (for example, the UV chromospheric network) are analogous and may be considered with the same or similar analysis, but other types of field (such as sunspot penumbrae) are likely too complex for simple analysis and require numerical modeling.

In this analysis we consider cross-correlation of an idealized small patch of quiet Sun with  $\pi r_p^2$  pixels, of nearly uniform intrinsic brightness everywhere except in a fraction  $f_d$  of the pixels of which are occupied by narrow, dark features with steep sides that are, on average,  $t_d$  pixels across, and an absolute intensity deficit of  $I_d$  (Figure . For typical quiet-Sun visible light observations,  $f_d$  is about 0.1 and  $I_d$  is about  $0.5 C$ . Assuming that the correlation algorithm does not ‘miss’ (it achieves

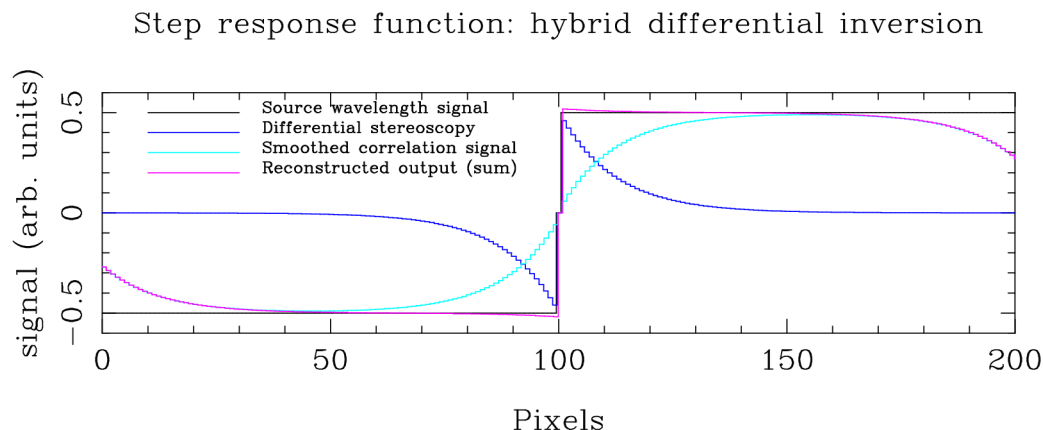


Fig. 1.— Step response of the filter in Eq. 5 shows how the different components of hybrid inversion combine to reconstruct the wavelength shift signal. The source wavelength (black) is a discrete Heaviside function with step at pixel 100. The differential stereoscopy step (in the absence of noise) yields a high-pass filtered version of the Heaviside function (blue), while the correlation step yields a low-pass filtered version (cyan). Because the filters are constructed mathematically to match one another, the sum of the two filters (magenta) reproduces the step. The low-pass curve suffers from edge effects at the far sides of the image, but in a typical detector with more than  $10^3$  pixel width, edge effects are minimal.

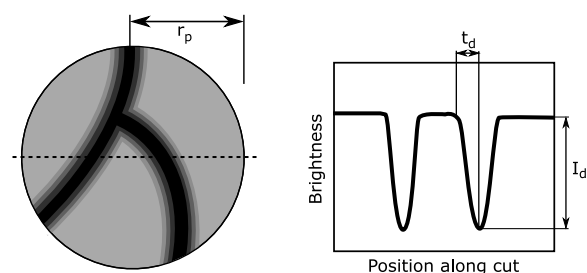


Fig. 2.— Sample correlation field used for our correlation photon analysis. Correlation between two images is used to align two patches of pixels with radius  $r_p$ . The image field consists of dark lanes against a background of approximately uniform brightness (left). The lanes consist of side-walls with thickness  $t_d$  and depth  $I_d$  (right). A fraction  $f_d$  of the image is considered to be lane wall.

a match between corresponding features in the opposite order images), we assume that errors in the resulting overall position of the patches is due to randomization errors from the displacements (real and apparent) of the dark features between the two images. In the worst non-pathological case, every intensity feature in the image patch is displaced by a different random amount, representing a strong high-spatial-frequency field. In that case, each feature’s apparent location is the incoherent sum of two random variable samples: one due to photon counting statistics in the sloping sides of the feature, and one due to the random displacements of the features themselves. The former depends on the steepness of feature sides, the overall brightness of the image, and the number of pixels in each feature wall. The latter depends on the dispersion of the instrument and the variability of spectral offset across the image

The uncertainty in location of each feature due to photon counting statistics is related to the slope at the sides of the feature: correlation fitting converts intensity in the sloping sides of a feature to position, so we can estimate the position/wavelength noise due to error in the intensity, by simply scaling the intensity noise to account for this conversion. The cross-correlation requires comparison between two features, so one can write:

$$\langle \Delta X_{ph,1} \rangle_{RMS} = \frac{t_d}{I_d} \langle \Delta I_{ds} \rangle_{RMS} = \frac{t_d}{I_d} I_0 \sqrt{\frac{2}{t_d n_{ph}} \left( \frac{2I_0}{2I_0 - I_d} \right)} \quad (11)$$

where  $\Delta I_{ds}$  is the uncertainty in brightness in the side-of-feature pixels, and the right-hand expression accounts for the typical number of pixels in the sides of a particular feature. The  $n_{ph}$  comes from the fraction  $\langle \Delta I \rangle_{RMS} / I_0$  and is the number of photons counted during the exposure. The unitless  $2I_0 / (2I_0 - I_d)$  arises because the average brightness in a feature sidewall is halfway between the background intensity and the dark feature intensity, The extra factor of 2 under the radical comes from the fact that the noise in offset is the incoherent sum of the location noise in each of the two features being compared.

The ensemble average error position  $\langle \Delta X_{ph} \rangle_{RMS}$  is then just the incoherent average of the offsets of each feature wall, or

$$\langle \Delta X_{ph} \rangle_{RMS} = \frac{2I_0}{I_d r_p} \sqrt{\frac{I_0 t_d}{\pi f_d n_{ph} (2I_0 - I_d)}} \quad (12)$$

Taking the patch to be about 15 pixels across, and assuming a scene of solar granulation with  $f_d = 0.05$ ,  $t_d = 2$ ,  $I_d = 0.5I_0$ , and  $n_{ph} = 5 \times 10^4$  yields a noise estimate of  $\langle \Delta X_{ph} \rangle_{RMS} = 2.4 \times 10^{-3}$  pixels. Photon noise in the correlation step is hence negligible compared to photon noise in the differential step. This is not surprising considering the large number of pixels that are averaged over by the correlation step. Put another way, the noise spectrum is dominated by high spatial frequencies, which are “smoothed out” by the correlation process.

### 2.3. Image noise in correlation stereoscopy

There is an additional source of error in the correlation step: because the wavelength signal  $\Lambda'(x)$  includes high spatial frequencies (the signal that is being measured by the differential stereoscopy step), different parts of the image must be shifted in different directions to find the average offset over the entire patch being correlated. These high spatial frequencies introduce an error into the measurement of the shifts  $X_{L,\pm 1}(x)$ , because the correlation step weights the importance of the different offsets according to the average sidewall slope in each portion of the patch being correlated, rather than uniformly throughout the patch of image. This error term is independent of the photon noise, and is introduced even for successful cross-correlations. It depends on the inequality of the weighting of the features, as well as the amount of displacement:

$$\langle \Delta X_{wgt} \rangle_{RMS} = \alpha \frac{\langle \overline{\delta \Lambda'_{patch} \delta |dI/dx|} \rangle_{RMS}}{\langle dI/dx \rangle_{RMS}} \quad (13)$$

where  $\delta$  is used to indicate actual differences from the patch-wide mean (different from  $\Delta$ , which is being used to indicate statistical error in a quantity),  $\Lambda'_{patch}$  is the signed difference between  $\Lambda'$  at each location in the patch being correlated and the mean for the whole patch,  $dI/dx$  is the slope of the intensity function at each location in the image, and  $\delta |dI/dx|$  is the difference between the current value of the slope and its patch-wide average. As above, angle-brackets symbolize RMS averaging over a complete data set; here, an over bar is used to represent signed averaging over the patch. The inclusion of both  $\delta$ -quantities (on the RHS) and  $\Delta$ -quantities (on the LHS) is because Eq. 13 describes errors in the measurement of  $X$  that are due to the interpretation of the images themselves even in the absence of injected noise, rather than to an injected noise source in the direct measurement of brightness in each image plane.

The numerator in the RHS of Eq. 13 depends only on the scene being viewed. The signed average simply applies an  $n_{samp}^{-1/2}$  scaling of the overall error term, according to the number of independent samples  $n_{samp}$  of image data in the patch. The quantity being averaged is the product of two random variables with zero mean and hence can be expanded simply in terms of their covariance  $C(x, y)$ :

$$\langle \Delta X_{wgt} \rangle_{RMS} = \frac{\alpha}{\langle dI/dx \rangle_{RMS} \sqrt{n_f}} \left( C(\delta \Lambda'_{patch}, \delta |dI/dx|) + \langle \delta \Lambda'_{patch} \rangle_{RMS} \langle \delta |dI/dx| \rangle_{RMS} \right) \quad (14)$$

where  $n_f$  is the number of “features” – separately resolved regions that each represents an independent sample of image data – in the patches being correlated.

Assuming that the wavelength and brightness signals are uncorrelated eliminates the covariance term:

$$\langle \Delta X_{wgt, uncorr} \rangle_{RMS} = \frac{\alpha \langle \delta \Lambda'_{patch} \rangle_{RMS} \langle \delta |dI/dx| \rangle_{RMS}}{\langle dI/dx \rangle_{RMS} \sqrt{n_f}} \quad (15)$$

so that, if wavelength and intensity of emissions be uncorrelated, the location uncertainty of a given cross-correlated patch is proportional to the RMS variation in central wavelength and the RMS variation in *slope* of the image intensity. For example, taking the patch to be about 15 pixels across,  $n_f = n_p/4$  (one unique feature every four pixels),  $\alpha \langle \delta \Lambda'_{patch} \rangle_{RMS} = 0.1$  pixel,  $\langle dI/dx \rangle_{RMS} = 0.2$ , and  $\langle \delta |dI/dx| \rangle_{RMS} = 0.1$  yields  $\langle \Delta X_{wtg,uncorr} \rangle_{RMS} = 0.006$  pixel.

In practice, the image intensity and wavelength variation are not completely uncorrelated. For example, small magnetic features tend to be found in dark intergranular lanes, rather than randomly across the quiet Sun, so that  $C(\delta \Lambda'_{patch}, \delta I) \neq 0$ . It is not clear, however, how or whether  $dI/dx$  and  $\Lambda'$  are correlated. In the worst case, they are proportional and the covariance term is equal to the product term in Eq.14, doubling the effective noise level from this source to (in the example) 0.012 pixel. In the best case,  $\delta \Lambda'$  would be near zero everywhere except where  $dI/dx$  is small. In that case, the covariance term would nearly exactly cancel the product term in Eq. 14 and eliminate this noise source.

In the context of a photospheric magnetograph, some further information about the covariance term may be used. In the quiet Sun for example, the strongest magnetic fields are observed to exist in the intergranular lanes, near local minima in continuum intensity. This suggests that the covariance between  $dI/dx$  and  $\delta \Lambda'_{patch}$  is in fact negative in real scenes of solar granulation, so that Eq. 15 likely overestimates the strength of this noise source in quiet sun magnetic measurements.

In scenes that contain more contrast, particularly magnetic-correlated contrast, image correlation problems can dominate the Zeeman shift signal. In particular, near sunspots very strong variations in intensity are strongly correlated to very strong variations in magnetic field, reducing the effectiveness of this technique for inverting stereoscopic data of sunspot fields. This was observed by DeForest et al. (2004), who found that correlation introduced strong artifacts into a not-well-resolved sunspot penumbra.

## 2.4. Image brightness gradients

Equation 2 includes several important engineered cancellations. Failure of those cancellations causes leakage of intensity or other information into the derived wavelength signal. The most important, and most likely to fail, cancellation is the elimination of an intensity spatial-derivative signal from the  $J$  introduced in Eq. 3. In the narrow-line approximation described by DeForest et al. (2004), the single-image brightness is given by (their equation 7):

$$I_n \approx \frac{[E_c \otimes F](x/\alpha_n)}{\alpha_n} - L(x) + \alpha_n L(x) \frac{d\Lambda'}{dx} + \alpha_n \Lambda'(x) \frac{dL}{dx} - 2\alpha_n^2 \Lambda'(x) \frac{dL}{dx} \frac{d\Lambda'}{dx} \quad (16)$$

(where, again,  $E_c$  is the continuum brightness per unit wavelength,  $F$  is the prefilter function,  $L(x)$  is the total line depth intensity, and  $\alpha_n$  is the dispersion of the  $n^{\text{th}}$  spectral order). The differential inversion arises from noticing that the difference between two opposite orders contains a useful  $d\Lambda'/dx$  term:

$$I_n(x) - I_{-n}(x) = 2\alpha_n L(x) \frac{d\Lambda'}{dx} + 2\alpha_n \Lambda'(x) \frac{dL}{dx} \quad (17)$$

in which the  $d\Lambda'/dx$  term is desired and the  $dL/dx$  term is undesired. In hybrid stereoscopy the images are resampled into  $X_L$  coordinates with the substitution:

$$X_{L,n} = x + \alpha_n \Lambda'_L(x) \quad (18)$$

that eliminates the undesired  $dL/dx$  term in Eq. 17 to first order. This process inevitably introduces some other undesired terms. In particular, substituting Eq. 18 into Eq. 16 yields (writing  $C_L(x)$  for the convolution term):

$$\begin{aligned} I_n(X_{L,n}) \approx & \left( C_L(x) + \alpha_n \Lambda'_L \frac{dC}{dx} \right) - \left( L(x) + \alpha_n \Lambda'_L \frac{dL}{dx} \right) \\ & + \left( \alpha_n L \frac{d\Lambda'}{dx} + \alpha_n^2 \Lambda'_L \frac{dL}{dx} \frac{d\Lambda'}{dx} + \alpha_n^2 \Lambda'_L \Lambda'_L \frac{d^2 L}{dx^2} \right) \\ & + \left( \alpha_n \Lambda'_L \frac{dL}{dx} + \alpha_n^2 \Lambda'_L \Lambda'_L \frac{d^2 L}{dx^2} + \alpha_n^2 \Lambda'_L \frac{d\Lambda'}{dx} \frac{dL}{dx} \right) \\ & - \left( 2\alpha_n^2 \Lambda'_L \frac{dL}{dx} \frac{d\Lambda'}{dx} + 2\alpha_n^3 \Lambda'_L \left( \left( \frac{d\Lambda'}{dx} \right)^2 \frac{dL}{dx} + \Lambda'_L \frac{d^2 L}{dx^2} \frac{d\Lambda'}{dx} + \Lambda'_L \frac{dL}{dx} \frac{d^2 \Lambda'}{dx^2} \right) \right) \end{aligned} \quad (19)$$

where  $C(x)$  is the convolution term from Eq. 16. As before, subtracting opposite orders removes all terms that contain an even power of  $\alpha$ , and doubles the remaining terms. Grouping all terms and discarding terms beyond first order in  $\Lambda'$  yields:

$$I_n(X_{L,n}) - I_{-n}(X_{L,-n}) \approx 2\alpha_n \left( L \frac{d\Lambda'}{dx} + \Lambda'_L \frac{dC_L}{dx} + \Lambda'_H \frac{dL}{dx} - 2\alpha_n^2 \left( \frac{d\Lambda'}{dx} \right)^2 \Lambda'_L \frac{dL}{dx} \right) \quad (20)$$

where the first term is desired and the other terms are noise. The  $dC_L/dx$  term is normally small both because the filter function is symmetric in wavelength and because the convolution integral smooths across several pixels. The  $\Lambda'_H$  term represents leakage of the  $dL/dx$  signal into the data. (Recall,  $\Lambda'_H$  is just the high spatial frequency component of the wavelength shift, given by  $\Lambda' - \Lambda'_L$ ). The low-frequency image contribution to the noise has been reduced by the square of the (normally small) factor  $\alpha_n d\Lambda'/dx$ .

The LHS of Equation 20 is merely the numerator of the  $J$  definition in Equation 3. The denominator is the sum of the two intensities, which retains the even powers of  $\alpha_n$  while canceling the odd powers. Again, many cancellations occur, leaving:

$$I_n(X_{L,n}) + I_{-n}(X_{L,n}) \approx 2 \left( C_L(x) - L + 2\alpha_n^2 \Lambda' \Lambda'_L \frac{d^2 L}{dx^2} \right) \quad (21)$$

so that the summed brightness of the resampled images has a systematic noise term that is proportional to the second derivative of the line depth. Combining the terms yields a more complete expression for  $J$ :

$$\begin{aligned} J &\approx \alpha_n \frac{L \frac{d\Lambda'}{dx} + \Lambda'_L \frac{dC_L}{dx} + \left( \Lambda'_H - \left( \alpha_n \frac{d\Lambda'}{dx} \right)^2 \Lambda'_L \right) \frac{dL}{dx}}{(C_L(x) - L) + 2\alpha_n^2 \Lambda' \Lambda'_L \frac{d^2 L}{dx^2}} \\ &\approx \alpha_n \frac{L}{C_L} \left( \frac{d\Lambda'}{dx} + \Lambda'_L \frac{dC_L}{L dx} + \left( \Lambda'_H - \left( \alpha_n \frac{d\Lambda'}{dx} \right)^2 \Lambda'_L \right) \frac{dL}{L dx} - \frac{2\alpha_n^2 \Lambda' \Lambda'_L}{C_L} \frac{d^2 L}{dx^2} \frac{d\Lambda'}{dx} \right) \end{aligned} \quad (22)$$

where first order approximations to the fraction have been taken, and squares of perturbations have been ignored. The first term of Eq. 22 reproduces the desired signal (Eq. 4) and the additional terms represent noise sources due to the image itself. Writing them as an error term  $\Delta J_{grad}$ ,

$$\Delta J_{grad} \approx \frac{\alpha_n \Lambda'_L}{C_L} \left( \frac{dC_L}{dx} + \left( \frac{\Lambda'_H}{\Lambda'_L} - \left( \alpha_n \frac{d\Lambda'}{dx} \right)^2 \right) \frac{dL}{dx} - 2\alpha_n \Lambda' \frac{d^2 L}{dx^2} J_{ideal} \right) \quad (23)$$

where the first terms represent leakage of intensity information into the wavelength signal (both from continuum variation and from line variation), and the final term represents leakage of rapid brightness variations into the J gain and is negligible in nearly all cases.

The continuum intensity leakage term is dependent on large-scale variations in continuum brightness, because  $C_L$  is smoothed (by convolution with the filter function) over a distance of  $\alpha_n \delta \lambda$ , where  $\delta \lambda$  is the width of the entrance filter. In typical applications,  $\alpha_n \delta \lambda$  might be 5-15 pixels. A scene of solar granulation with  $C/L \sim 10$ ,  $\alpha \Lambda'_L \sim 0.1$  pixel and  $\alpha_n \delta \lambda \sim 10$  pixels, with intergranular lanes 3 pixels wide and continuum dips of 30% in the lanes, will have a continuum intensity leakage error of  $\sim 5 \times 10^{-4}$  in J/I in the regions on either side of the lane, equivalent to the noise from  $10^6$  photons. The error accumulates coherently over half of the dispersed filter width, or about 5 pixels, yielding a peak injected noise signal in  $\alpha \Lambda'$  of  $\sim 0.025$  pixel in the lane center from just the continuum term.

The continuum intensity leakage is much stronger in regions with strong large scale variations in intensity, coupled with strong line shifts (such as found in sunspots). In a sunspot scene with  $C/L \sim 10$ ,  $\alpha \Lambda'_L \sim 4$  pixels, and a continuum dip of 75% within the sunspot, pixels near the sunspot edge will have a continuum leakage term of 0.2 in J/I, much larger than any photon noise in the

system. The error accumulates coherently for the full dispersed width of the entrance filter, yielding integrated errors in  $\alpha\Lambda'_L$  as high as 20 pixels near the edge of the sunspot. This large error injection is the primary reason why DeForest et al. (2004) found sunspot measurements to be challenging with this inversion technique.

The line intensity leakage term is largest in regions of very rapid variation of the central wavelength, but is negligible compared to the continuum leakage in most scenes. Considering a “challenging” scene of solar plage with  $\alpha\Lambda'_L \sim 1$  pixel,  $\alpha\Lambda'_H \sim 0.3$  pixel amplitude,  $\alpha d\Lambda'/dx \sim 0.1$ ,  $C/L \sim 10$ , and  $dL/Ldx \sim 0.5/\text{pixel}$  yields intensity leakage of about  $7 \times 10^{-3}$  into J/I from the central term. This is equivalent to the photon noise from  $3 \times 10^4$  photons, and if sustained across a full correlation patch of width 15 pixels could inject an error signal of up to  $\sim 0.1$  pixel into the final inversion; this represents about 20% of the background field. With a more typical quiet-Sun case of  $\alpha\Lambda'_L < 0.1$  pixel (30 G),  $\alpha\Lambda'_H \sim 0.1$  pixel, and  $\alpha d\Lambda'/dL \sim 0.02$ , the intensity leakage noise is under  $10^{-3}$  in J/I and thus leads to errors of under 0.015 pixel after accumulating over a 15-pixel FWHM patch.

The rapid brightness variation leakage depends on rapid changes in the line depth, in regions that are magnetized. It is negligible in nearly all cases other than sunspot penumbrae. In the quiet Sun, the strongest value of the term occurs where  $g$ -band bright points are present in intergranular lanes. In a typical  $g$ -band bright point, with  $\alpha\Lambda' \sim 1$  pixel,  $\alpha\Lambda'_L \sim 0.1$  pixel and  $d^2L/dx^2 \sim 0.005I \text{ pixel}^{-2}$ ,  $J$  can be expected to have a relative error of only  $1 \times 10^{-3}$  from this term. In sunspot penumbrae, where both  $\alpha\Lambda'_L$  and  $\alpha\Lambda'$  may be larger than order unity, and where  $d^2L/dx^2$  may be a factor of 4-10 higher than in intergranular lanes due to the fine nature of penumbral roll structure,  $J$  can be expected to have a relative error of order close to unity from this term, severely degrading results in sunspot penumbrae even if the continuum leakage signal (above) were not a problem.

In all cases, the intensity gradient leakage terms are proportional to  $\Lambda'$  and therefore represent a gain error rather than an uncorrelated additive noise source that affects detection of lone magnetic features.

## 2.5. Filter passband gradients

Filter passband gradients enter because the overall measured intensity is affected by the throughput function of the prefilter. In conventional filtergraph instruments, the slope of the side-lobes of the main filter passband is used to convert wavelength offset into an intensity signal; in stereographic instruments, that signal is undesired and represents a source of noise. Even in a properly tuned stereoscopic instrument, large excursions of  $\Lambda'$  carry the spectral line out of the

flat central region of the prefilter's passband and into the sloping wings. This modifies Eq. 16, to include the effect of the filter on the measured  $L(x)$ :

$$I_n \approx \left\{ \begin{array}{l} \frac{[E_c \otimes F](x/\alpha_n)}{\alpha_n} - L(x)F(\Lambda') + \alpha_n L(x)F(\Lambda') \frac{d\Lambda'}{dx} \\ + \alpha_n \Lambda'(x) \left( F(\Lambda') \frac{dL}{dx} + L(x) \frac{dF}{d\Lambda'} \frac{d\Lambda'}{dx} \right) \\ - 2\alpha_n^2 \Lambda'(x) \left( F(\Lambda') \frac{dL}{dx} \frac{d\Lambda'}{dx} + L(x) \frac{dF}{d\Lambda'} \left( \frac{d\Lambda'}{dx} \right)^2 \right) \end{array} \right\} \quad (24)$$

where  $F(0)$  is taken to be unity. Of the two new terms, only one is asymmetric, so the difference equation becomes:

$$I_n - I_{-n} = F(\Lambda'(x)) \left( 2\alpha_n L(x) \left( 1 + \frac{\Lambda'}{F(\Lambda'(x))} \frac{dF}{d\Lambda'} \right) \frac{d\Lambda'}{dx} + 2\alpha_n \Lambda'(x) \frac{dL}{dx} \right) \quad (25)$$

where both the overall factor of  $F$  and the additional unitless derivative  $(\Lambda'/F)(dF/d\Lambda')$  represent perturbations on the gain of the measured  $d\Lambda'/dx$ , and the final term is the intensity leakage that is removed by the hybridization step in the overall inversion. In a well-tuned instrument, the maximum value of  $F$  occurs near  $\Lambda' = 0$ , so we may expand  $F$  and  $F'$  around that value:

$$F \approx 1 - \frac{1}{2} \left( \frac{\Lambda' - \Lambda'_{filt}}{W} \right)^2 \quad (26)$$

where  $\Lambda'_{filt}$  is the difference between the center wavelength of the filter and the rest wavelength of the spectral line, and  $W$  is the half-width at half maximum of the filter passband. Then the derivative  $dF/d\Lambda'$  is given by  $(\Lambda'_{filt} - \Lambda')/W$ . As an example, if  $\Lambda'_{filt}$  is about  $-W/10$  and  $\Lambda'$  is about  $W/4$ , this yields a gain error of 7% in the  $d\Lambda'/dx$  signal.

## 2.6. Rapid variation of central wavelength

Rapid variation of the central wavelength of the observed spectral line affects the measured signal from differential stereoscopy. The differential inversion (Eq. 5) is derived using a first-order expansion of the brightness in terms of the slope  $d\Lambda'/dx$  of the central wavelength versus position. If the condition  $d\Lambda'/dx \ll \alpha_n^{-1}$  does not hold (the slope is significant compared to the reciprocal of the instrument's dispersion) then the differential inversion equation is not valid and the derived  $\Lambda'_{c1}$  will differ from the true  $\Lambda'$  even in the absence of any other noise source. This is due to the effect being exploited to extract the  $d\Lambda'/dx$  signal from the intensities: small shifts in the  $\lambda$  direction project into the dispersed spatial direction, so that the line of integration in the  $(x, \lambda)$  plane that contributes to a single pixel may have more or less contribution from the line core depending on the relative angle between  $\alpha_n$  and  $d\Lambda'/dx$ . The resultant variation in intensity is extremely nonlinear when  $\alpha_n$  and  $d\Lambda'/dx$  are nearly parallel. Further, the  $d\Lambda'/dx$  intensity variations are due to small

shifts in image position as  $\Lambda'$  varies. If  $\Lambda'$  grows larger than  $1 \text{ pix}/\alpha_n$ , then the image shift becomes noticeable and distorts the resultant line-shift images.

The various effects of large excursions in  $\Lambda'$  on spatial distributions are illustrated in Figure 3, which illustrates the geometry of the  $(x, \lambda)$  plane in a stereoscopic measurement of line center for a spectral line with structured Doppler signal. Three forms of perturbation on the line are shown: a sinusoidal modulation of the line center wavelength; a triangle wave modulation; and a dual step function. The sinusoidal modulation fits the criteria outlined by DeForest et al. (2004) for differential stereoscopic inversion:  $\alpha_n d\Lambda'/dx \gg 1$  and  $\alpha_n \Lambda'$  is not large compared to the spatial features of interest. The others fail in different ways. The triangle wave fails because  $\alpha_n d\Lambda'/dx \sim 1$ , and the offset fails because  $\alpha_n \Lambda'$  is large compared to the width of the transition features at the edges of the step in central wavelength.

Hybrid differential stereoscopy reduces the effects by eliminating the low spatial frequency components, so that the amplitude and slope of the high spatial frequency component  $\Lambda'_H$ , rather than of  $\Lambda'$  itself, are of import: structures larger than roughly the width of the patch used for correlation are attenuated or eliminated by the high-pass filtering that generates  $\Lambda'_H$ .

By considering carefully the geometry of the differential inversion in the  $(x, \lambda)$  plane it is possible to estimate the systematic errors due to slope and line-displacement effects alone on differential stereoscopy, even in the absence of image effects such as variations in line or continuum intensity. Figure 4 shows the geometry of dispersed integration through a spectral line. The contribution  $L'_n$  to the measured intensity  $I_n$  is approximated to first order in Eq. 4, but the contribution may also be written exactly in the case of constant  $L(x)$ , constant  $d\Lambda'/dx$ , and a broad filter:

$$I_n(x) = \int d\lambda (F(\lambda') E_c(x - \alpha_n \lambda') - L \delta(\lambda - \Lambda'(x) + (\alpha_n \lambda) d\Lambda'/dx) = C - \frac{L}{1 + \alpha_n (d\Lambda'/dx)} \quad (27)$$

Applying this expression to Eq. 3 gives an analytic formula for the relation between  $J$  and  $d\Lambda'/dx$ . Letting  $\gamma \equiv \alpha_n d\Lambda'/dx$  and  $\ell \equiv L/C$ ,

$$J_n = \frac{I_n - I_{-n}}{I_n + I_{-n}} = -\gamma \left( \frac{\ell}{1 - \ell} \right) \left( \frac{1}{1 - (\gamma^2/(1 - \ell))} \right) \quad (28)$$

where the factor  $\alpha_n \ell/(1 - \ell)$  is a linear calibration coefficient on  $d\Lambda'/dx$  and the right-hand term is a nonlinearity term. The nonlinearity in  $J_n$  becomes strongly evident when  $\gamma$  grows to about 0.5, where (with  $L/C = 0.1$ ) the nonlinearity term has a value of 1.38, and grows to infinity where  $\gamma = \sqrt{1 - \ell}$ .

The strong nonlinearity in  $J$  is partially compensated by spatial distortion. The nonlinear term causes growth in  $J$  compared to the proportionality with  $d\Lambda'/dx$ , but that growth is accompanied by spatial distortions that partially cancel the nonlinearity. In particular, the measurable quantity of

interest is  $\Lambda'$  rather than  $d\Lambda'/dx$ . In a pure differential inversion, with  $\gamma$  positive and non-negligible, the  $J_n$  signal arises from a slight weakening of the spectral line in the  $-n$  spectral order and a strong strengthening in the  $+n$  order. However, the image in the  $+n$  channel is strongly foreshortened while the image in the  $-n$  channel is weakly fore-lengthened: the total  $x$ -integrated intensity in each spectral order remains the same under small to moderate ( $<1$  pixel)  $\Lambda'$  perturbations in the image.

Consider a finite shift in central wavelength  $\Lambda'$  as illustrated in Figure 4. Accompanying the shift in brightness is a spatial distortion that affects the two spectral orders differently. In the positive order the line depth is more strongly expressed, because it is concentrated into fewer pixels than might be expected from the spatial extent of the feature. Likewise, in the negative order the line depth is more weakly expressed, because it is spread across more pixels than the usual spatial extent of the feature. The corresponding variation of  $J_n$  thus has three regimes in this simple system (neglecting the line width):

$$J_n = \begin{cases} |x| > \frac{\delta x + \alpha_n \delta \Lambda}{2} & 0 \\ \frac{\delta x - \alpha_n \delta \Lambda}{2} \geq |x| > \delta x - \frac{\alpha_n \delta \Lambda}{2} & J_{mid} = \frac{I_0 - I_{-n,l}}{I_0 + I_{-n,l}} \\ \frac{\delta x - \alpha_n \delta \Lambda}{2} > |x| & J_{ctr} = \frac{I_{n,l} - I_{-n,l}}{I_{n,l} + I_{-n,l}} \end{cases} \quad (29)$$

where (from Eq. 27)  $I_0 = C - L$ ,  $I_{-n,l} = C - L/(1 + \gamma)$ , and  $I_{n,l} = C - L/(1 - \gamma)$ . Simple analysis shows that

$$J_{mid} = \frac{-\gamma}{(1 + \gamma)(2/\ell - 1) - 1} \quad (30)$$

and

$$J_{ctr} = \frac{-\gamma}{(1 - \gamma^2)/\ell - 1}, \quad (31)$$

so that the measured wavelength shift may be computed directly:

$$\delta \Lambda_{meas.} \equiv -\alpha_n^{-1} \frac{C}{L} \int J_n dx \quad (32)$$

$$\begin{aligned} &= -\alpha_n^{-1} \ell^{-1} \left\{ 2\alpha_n \delta \Lambda \left( \frac{-\gamma \ell}{(2 - \gamma)(1 - \ell) - \gamma} \right) + \delta x (1 - \gamma) \left( \frac{-\gamma \ell}{(1 - \gamma^2) - \ell} \right) \right\} \\ &= \left\{ \left( \frac{2\gamma \delta \Lambda}{(2 - \gamma)(1 - \ell) - \gamma} \right) + \frac{(\delta x \alpha_n^{-1})(1 - \gamma)(\gamma)}{1 - \ell - \gamma^2} \right\} \\ &= \delta \Lambda \left\{ \frac{1}{1 - \ell} \right\} \left\{ \frac{\gamma}{1 + \gamma(1 + \ell/2)} + \frac{(1 - \ell)(1 - \gamma)}{1 - \ell - \gamma^2} \right\} \quad (33) \end{aligned}$$

$$\approx \delta \Lambda \left\{ \frac{1}{1 - \ell} \right\} \left\{ \left( 1 - \frac{\ell \gamma}{1 - \ell} \right) \right\} \quad (34)$$

where the last row expands the  $\gamma$ -dependent error factor to first order in  $\gamma$ . Equation 34 shows that the linear approximations used to derive 2 are quite good, at least for this simple geometry: the first nontrivial term in the error factor is two orders of approximation smaller than the extracted signal (taking both  $\gamma$  and  $\ell$  to be small, as did DeForest et al. 2004). The high quality of the approximation can be seen in Figure 3: the measured peak and feature-averaged  $\Delta\Lambda_{meas}$  in each feature remains close to the injected  $\Delta\Lambda$  of the model, despite gross violation of the assumptions used to derive Equation 2.

The astute reader will have noticed that Equation 33 has a pole at  $\gamma = \sqrt{1 - \ell}$ . That is because we have neglected finite length effects in the region where the line shift occurs. Equation 33 is more complex but exact for this geometry, provided that the line width is small compared to  $\delta x / \alpha_n$ . When that condition is violated (which happens when the center locus is exceptionally narrow on the detector), individual pixel lines of integration do not integrate across the entire foreshortened spectral line but are limited instead by the ends of the spectral feature. This limitation keeps the signal response  $J_{ctr}$  finite. Equation 33 neglects this effect, leading to a spurious pole.

For nonzero line widths, Equation 33 reveals a constant correction factor of  $1/(1 - \ell)$  that must be applied to stereoscopic inversions in general. This correction (of order 10%) is a true calibration coefficient, in the sense that it is independent of  $\gamma$ .

### 3. Summary & Specific Observing Scenario

The effects in §2 above separate into two primary classes: additive and multiplicative noise in the data. The additive effects, such as photon noise, affect sensitivity for detection of small magnetic or Doppler features; the multiplicative effects, affect the precision of magnetic measurements. Here we calculate a noise budget for a plausible observing scenario using a stereoscopic instrument as a photospheric magnetograph.

Consider an instrument observing quiet sun through the Dunn Solar Telescope (DST; Dunn 1969) and the medium-order adaptive optics system (Rimmele 2004), at the Fe I 617.34 nm line, with 0.07 arcsec pixels (the diffraction limit is 0.2 arcsec), a 67 pm prefilter passband width detuned from  $\Lambda_0$  by 6.7 pm (10% of the bandwidth),  $\ell = 0.1$ , dispersion  $\alpha = 100 \text{ pixel nm}^{-1}$ ,  $n_{ph} = 5 \times 10^4$  photons per pixel, and a correlation patch FWHM of 15 pixels ( $\epsilon = 0.09$ ). Consider that a “typical” resolved feature strength is between 100G-1kG, with length scales of a few pixels (so that only stereoscopic measurements apply, without the stabilizing influence of the more precise correlation stereoscopy). The 617.34 nm line has a Landé  $g$  factor of 2.5, so that the Zeeman splitting equation is just ‘

$$B' = \frac{hc}{4\Lambda_0^2 g \mu} (\delta' \Lambda) = 5.6 T \text{ nm}^{-1} \delta' \Lambda = 5.6 \text{ kG}^{-1} \delta' \Lambda \quad (35)$$

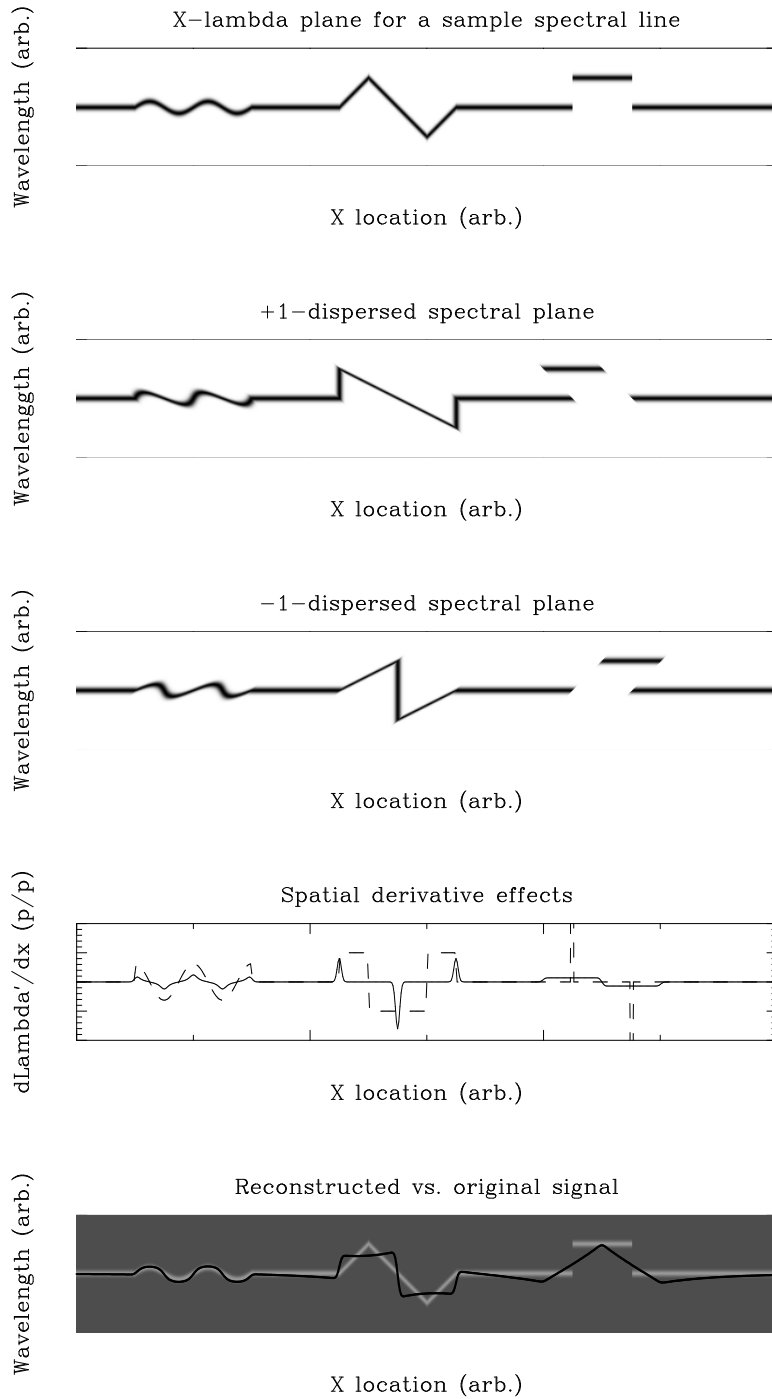


Fig. 3.— Five plots showing arbitrary variations of spectral line central wavelength show the manner in which the approximation of Equation 5 breaks down at high line slopes. In order: the X-Lambda plane; the X-lambda plane, dispersed in two opposite directions (Pixel brightnesses are formed by vertical integration in these two plots); the original and derived spatial derivative of line center wavelength; and an overlay of the original and reconstructed signals. The sinusoidal segment at left is well matched. The pathological sawtooth and square wave segments are distorted by the coupling between wavelength and spatial position.

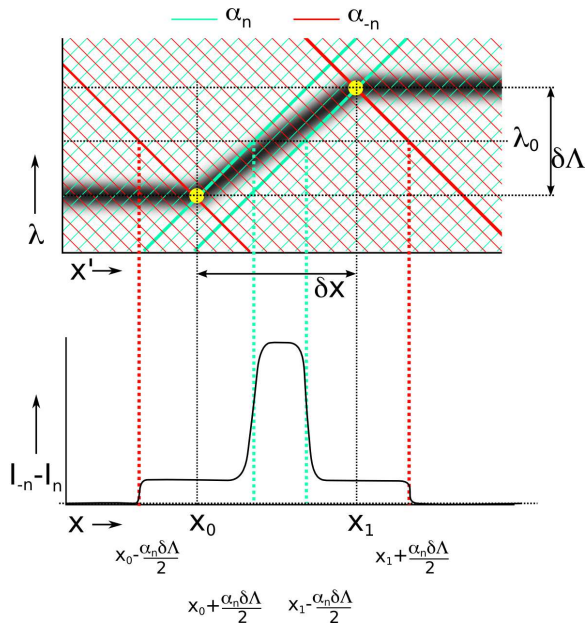


Fig. 4.— A finite linear feature in  $\Lambda_0$  demonstrates the interplay between projection, brightness, and feature size in a stereoscopic instrument. At top, a spectral line undergoes a finite shift  $\delta\Lambda$  between the points  $x'_0$  and  $x'_1$  in the  $(x', \lambda)$  plane. The instrument collects two spectral orders with dispersion  $\alpha_{\pm n}$ . Each order integrates pixels along lines of the appropriate slope: positive (cyan) or negative (red) and projects onto the detector  $x$  coordinate. At bottom the line depth brightness integral  $-(I_n - I_{-n})$  varies as a function of pixel location (projected back to the  $\lambda = \Lambda_0$  line at top).

where  $B'$  is measured resolution-smoothed magnetic field strength (“flux density”),  $h$  is Planck’s constant,  $c$  is the speed of light,  $g$  is the Landé factor,  $\mu$  is the Bohr magneton, and  $\delta'\Lambda$  is the *splitting* of the line (twice the shift). The splitting measurement is the result of *two* independent measurements of a shift  $\Delta\Lambda$ : one in right-circularly polarized light (Stokes I+V) and one in left-circularly polarized light (Stokes I-V). Hence the noise  $\Delta B'$  is a factor of  $\sqrt{2}$  higher than might be supposed by simple scaling of the  $\Delta\Lambda$  noise terms in §2 with Equation 35.

The noise budget for a quiet-Sun DST observation may be summarized as in -Table 1. Two principal types of error enter into the measurement: random or quasi-random noise as described in §§2.1-2.4; and calibration nonlinearities that enter as a result of filter detuning and the first-order stereoscopic inversion as described in §§2.5-2.6.

Because of the multiple sources of error, calculation of error budgets for actual observations must be carried out on a case-by-case basis; however, we note that for magnetograph observations of the photosphere, the dominant noise term is (as expected) photon noise for a plausible instrument setup and a range of targets that includes most non-sunspot-related targets on the Sun. The expected formal single-exposure magnetogram sensitivity is  $\sim 10$  Gauss (twice the RMS background noise level) and the expected magnetic flux calibration accuracy is expected to be close to 10% in most cases including plage.

The error budget in Table 1 is broadly consistent with test measurements collected by DeForest et al. (2004) at the Dunn Solar Telescope. In those measurements, exposures of only  $\sim 8 \times 10^3$  photons were collected; 16 exposures were combined to create each image for an effective exposure of  $1.2 \times 10^5$  photons; and an *asymmetric* inversion (whose sensitivity was reduced by a factor of  $\sqrt{2}$  compared to the symmetric inversion discussed here) was used. The resulting calculated photon noise level is thus a factor of  $\sqrt{24/5}$  higher than shown here, or 9.5 G (0.45 G for the correlation noise), and the non-photon noise sources are scaled up a factor of  $\sqrt{2}$  compared to the sample measurement described here. This leads to a total *a priori* noise level estimate of 10 G for that measurement. Indeed, in a small quiet region with no detected flux features, DeForest et al. found *a posteriori* RMS noise levels between 9-12 Gauss, in good agreement with the current *a priori* calculation.

#### 4. Conclusions

We have calculated a detailed noise budget for hybrid differential inversion of the line-shift signal from a stereoscopic spectrograph, with specific application as a stereoscopic magnetograph observing a specific absorption line (Fe I 617.34 nm) in the solar photosphere. The noise budget is photon dominated and careful *a priori* analysis shows that it offers similar calibration performance

to existing and past filtergraph (SOHO/MDI, Scherrer et al. 1995) and Fourier tachometer (GONG; Leibacher 1999) instruments (Jones and Ceja 2001): instrument response to field is within a few to ten percent of linear over a wide range of pixel-averaged field strengths.

The principal difference between the stereoscopic technique and the filtergraph or Fourier tachometer techniques is that the instrument can operate much more rapidly, because all required photons are collected simultaneously in a dual-polarized-beam instrument. This is very important for ground based observations in which atmospheric seeing effects severely limit the precision with which line shifts can be measured in time-multiplexing instruments such as filtergraphs.

Some instruments, such as ZIMPOL (Povel 1998), have been able to limit crosstalk of atmospheric effects by multiplexing extremely rapidly; but such instruments are still subject to motion blur even in the absence of severe crosstalk. A stereoscopic spectral imager should be able to acquire a diffraction limited magnetogram with few-Gauss sensitivity in a small fraction of a second at most major observing facilities. We expect this rapidity of acquisition to become important even in space-based observing as higher resolution instruments (e.g. *Hinode/SOT*; Ichimoto et al. 2006) release data to the scientific community: the race between solar evolution and data acquisition (photon counting) give rise to a tradeoff between sensitivity and spatial resolution for any spectral imager, even above the atmosphere.

Particularly for features that are spatially small, stereoscopic imagers offer a surprising advantage: because the fundamental signal extracted from the images is proportional to the *spatial derivative* of the line shift signal, such instruments are particularly sensitive to small features, right down to the spatial resolution of the measurement. Like Dolby<sup>TM</sup> noise reduction for audio recordings (e.g. Vaseghi 2006), spatial derivative measurement enhances high spatial frequencies, boosting the high frequency signal relative to the photon noise floor. Conventional spectral measurements sample each location in the image plane independently, so that in a roughly circular feature of linear size  $L$  and area  $A$  the uncertainty due to photon counting in the feature's total magnetic flux scales as  $A^{-1/2}$  or  $L^{-1}$ . In a differential stereoscopic measurement, the *average slope* uncertainty, rather than the total flux uncertainty, scales as  $L^{-1}$  so the total flux uncertainty is independent of feature size for features smaller than the correlation patches described in Section 3.

Stereoscopic spectral imaging is a special case of the more general technique of *spectral tomography* (e.g. Wilson et al. 1997), and appears to offer significant advantages in the regime we have described: observations of a narrow spectral line, where only one or two moments of the line are desired to be measured. Spectral tomography using regularized inverse or conjugate analysis techniques (e.g. Claerbout and Fomel 2004) could potentially be used to extract much more information about the spectrum, using multiple orders or, as did Wilson et al., crossed gratings; but as the number of additional channels grows, so do the potential paths for signal contamination

and crosstalk between different aspects of the measured spectrum. We conclude that stereoscopic techniques represent a sweet spot for imaged Doppler or magnetic measurements of solar scenes, offering superior photon efficiency and comparable performance to filtergraph measurements. This is already important as ground-based spectral imagers are already photon-starved near the diffraction limit in existing meter-class telescopes (such as the Dunn Solar Telescope, Dunn 1969, and the Swedish Vacuum Tower, Scharmer et al. 2003) and will grow more so near the diffraction limit of future telescopes such as the four-meter Advanced Technology Solar Telescope (Keller et al. 2002).

The authors thank Jack Harvey for helpful discussion of the current state of magnetograph cross-calibration, and Steve Tomczyk for pointing out the necessity of this paper. This work was funded internally by the Southwest Research Institute.

## REFERENCES

- J. C. Claerbout and S. Fomel. *Image Estimation by Example: Geophysical Soundings Image Construction and Multidimensional Autoregression*. Stanford University Press, Palo Alto, 3.4 edition, 2004.
- C. DeForest, D. F. Elmore, M. P. Bradford, J. Elrod, and D. L. Gilliam. Stereoscopic Spectroscopy for Efficient Spectral Imaging and Magnetography. *ApJ*, 616:600, November 2004.
- E. L. Dereniak. Infrared spectro-polarimeter. In *Integrated Optics: Theory and Applications*. Edited by Pustelny, Tadeusz; Lambeck, Paul V.; Gorecki, Christophe. *Proceedings of the SPIE, Volume 5957*, pp. 202-211 (2005)., 2005.
- R. B. Dunn. Sacramento Peak’s New Solar Telescope. *S&T*, 38:368, December 1969.
- J. L. Fox, C. C. Kankelborg, and T. R. Metcalf. Data inversion for the Multi-Order Solar Extreme-Ultraviolet Spectrograph. In *Optical Spectroscopic Techniques and Instrumentation for Atmospheric and Space Research V*. Edited by Larar, Allen M.; Shaw, Joseph A.; Sun, Zhaobo. *Proceedings of the SPIE, Volume 5157*, pp. 124-132 (2003)., 2003.
- K. Ichimoto, Y. Suematsu, T. Shimizu, Y. Katsukawa, S. Tsuneta, T. D. Tarbell, R. A. Shine, C. M. Hoffmann, A. M. Title, B. W. Lites, D. F. Elmore, and K. V. Strander. Magnetic Field Diagnostic Capability of Solar-B/SOT: Filtergraph Instrument. In *Astronomical Society of the Pacific Conference Series*, 2006.
- H. P. Jones and J. A. Ceja. Preliminary Comparison of Magnetograms from KPVT/SPM, SOHO/MDI and GONG+. In *Advanced Solar Polarimetry – Theory, Observation, and Instrumentation*, 2001.

- C. C. Kankelborg and J. L. Fox. First Results from the Multiple Order Stereoscopic EUV Spectrograph. *ApJ*, in prep., 2007.
- C. C. Kankelborg, P. C. Martens, and R. J. Thomas. Simultaneous EUV imaging and spectroscopy. In *ESA SP-493: Solar encounter. Proceedings of the First Solar Orbiter Workshop*, page 257, September 2001.
- C. U. Keller, T. R. Rimmele, F. Hill, S. L. Keil, J. M. Oschmann, and the ATST Team. The Advanced Technology Solar Telescope. *Astronomische Nachrichten*, 323:294–298, July 2002. doi: 10.1002/1521-3994(200208)323:3/4.
- J. W. Leibacher. The global oscillation network group (GONG) project. *Advances in Space Research*, 24:173–176, 1999.
- B. H. Miles. *Computed-tomography imaging spectropolarimeter*. PhD thesis, AA(THE UNIVERSITY OF ARIZONA), 1999.
- B. H. Miles, R. A. Goodson, E. L. Dereniak, and M. R. Descour. Computed-tomography imaging spectropolarimeter (CTISP): instrument design, operation, and results. In *Proc. SPIE Vol. 3753, p. 169-179, Imaging Spectrometry V, Michael R. Descour; Sylvia S. Shen; Eds.*, 1999.
- H. P. Povel. The Zurich Imaging Polarimeter (ZIMPOL). In *Astronomische Gesellschaft Meeting Abstracts*, 1998.
- T. R. Rimmele. Recent advances in solar adaptive optics. In D. Bonaccini Calia, B. L. Ellerbroek, and R. Ragazzoni, editors, *Advancements in Adaptive Optics. Edited by Domenico B. Calia, Brent L. Ellerbroek, and Roberto Ragazzoni. Proceedings of the SPIE, Volume 5490, pp. 34-46 (2004).*, page 34, October 2004.
- G. B. Scharmer, K. Bjelksjo, T. K. Korhonen, B. Lindberg, and B. Petterson. The 1-meter Swedish solar telescope. In *Innovative Telescopes and Instrumentation for Solar Astrophysics. Edited by Stephen L. Keil, Sergey V. Avakyan . Proceedings of the SPIE, Volume 4853, pp. 341-350 (2003).*, 2003.
- P. H. Scherrer, R. S. Bogart, R. I. Bush, J. T. Hoeksema, A. G. Kosovichev, J. Schou, W. Rosenberg, L. Springer, T. D. Tarbell, A. Title, C. J. Wolfson, I. Zayer, and MDI Engineering Team. The Solar Oscillations Investigation - Michelson Doppler Imager. *Sol. Phys.*, 162:129–188, 1995.
- S. V. Vaseghi. *Advanced Digital Signal Processing and Noise Reduction*. Wiley, New York, 3 edition, 2006.

D. W. Wilson, P. D. Maker, and R. E. Muller. Reconstructions of computed-tomography imaging spectrometer image cubes using calculated system matrices. In *Proc. SPIE Vol. 3118*, p. 184-193, *Imaging Spectrometry III*, Michael R. Descour; Sylvia S. Shen; Eds., 1997.

Source	Eq./Section	$\Delta\Lambda$ RMS (pm)	$\Delta B'$ RMS (G)	cal. err.
Photon noise (diff.)	9/§2.1	0.53	4.2	-
Photon noise (corr.)	12/§2.2	0.024	0.2	-
Image noise (corr.)	14/§2.3	0.12	1.0	-
Continuum leakage	23/§2.4	0.25	2.0	-
Line leakage	23/§2.4	0.15	1.2	-
Filter signal leakage	25/§2.5	-	-	3%-7%
Stereo nonlinearity	34/§2.6	-	-	1%-10%
TOTAL (in quadrature)	-	0.62	4.9	3%-12%

Table 1: Noise budget for a sample stereoscopic magnetograph measurement as described in the text. This measurement would have  $\sim 6$  G RMS noise even in field-free regions of the Sun, and 3%-12% calibration errors in the measured flux of small magnetized regions of 100-1000 G, no more than a few pixels across.